# The origins of intra- and inter-molecular vibrational couplings: A case study of H$_2$O-Ar on full and reduced-dimensional potential energy surface

Dan Hou, Yong-Tao Ma, Xiao-Long Zhang, and Hui Li

---

**Articles you may be interested in**

---

# The origins of intra- and inter-molecular vibrational couplings: A case study of H2O-Ar on full and reduced-dimensional potential energy surface

Dan Hou, Yong-Tao Ma, Xiao-Long Zhang, and Hui Li[a]
*Institute of Theoretical Chemistry, Jilin University, 2519 Jiefang Road, Changchun 130023,
People's Republic of China*

The origin and strength of intra- and inter-molecular vibrational coupling is difficult to probe by direct experimental observations. However, explicitly including or not including some specific intramolecular vibrational modes to study intermolecular interaction provides a precise theoretical way to examine the effects of anharmonic coupling between modes. In this work, a full-dimension intra- and inter-molecular *ab initio* potential energy surface (PES) for $H_2O$–Ar, which explicitly incorporates interdependence on the intramolecular $(Q_1, Q_2, Q_3)$ normal-mode coordinates of the $H_2O$ monomer, has been calculated. In addition, four analytic vibrational-quantum-state-specific PESs are obtained by least-squares fitting vibrationally averaged interaction energies for the $(v_1, v_2, v_3)$ = $(0, 0, 0), (0, 0, 1), (1, 0, 0), (0, 1, 0)$ states of $H_2O$ to the three-dimensional Morse/long-range potential function. Each vibrationally averaged PES fitted to 442 points has root-mean-square (rms) deviation smaller than 0.15 cm$^{-1}$, and required only 58 parameters. With the 3D PESs of $H_2O$–Ar dimer system, we employed the combined radial discrete variable representation/angular finite basis representation method and Lanczos algorithm to calculate rovibrational energy levels. This showed that the resulting vibrationally averaged PESs provide good representations of the experimental infrared data, with rms discrepancies smaller than 0.02 cm$^{-1}$ for all three rotational branches of the asymmetric stretch fundamental transitions. The infrared band origin shifts associated with three fundamental bands of $H_2O$ in $H_2O$–Ar complex are predicted for the first time and are found to be in good agreement with the (extrapolated) experimental values. Upon introduction of additional intramolecular degrees of freedom into the intermolecular potential energy surface, there is clear spectroscopic evidence of intra- and intermolecular vibrational couplings. © 2016 AIP Publishing LLC. [http://dx.doi.org/10.1063/1.4939089]

## I. INTRODUCTION

Water exists extensively in nature and most chemical reactions happen under aqueous conditions. Different from other liquids, the vibrational motions of water span an enormous range of frequencies and timescales, due to complicated intra- and intermolecular vibrational coupling and relaxations.[1–3] The complexes formed between water molecule with itself and other species have attracted considerable interest in physics, chemistry, and biology. Among them, the $H_2O$–Ar complex is one of the simplest systems which is capable of manifesting the effects of "hydrophobic interactions."[4,5] In addition, $H_2O$–Ar is of fundamental interest[6–10] because it is a model for the intermolecular potential and rovibrational states of atom-asymmetric top van der Waals complexes for studying the mixed character of all intra- and intermolecular vibrations. The infrared (IR) spectrum of the stretching and bending vibrations of $H_2O$ is one of the most direct probes of the dynamics of the $H_2O$–Ar complex of $H_2O$ doped in larger $(Ar)_N$ clusters, as it reflects the effects of solvation structures and the intermolecular forces.

The first far infrared spectrum of a $H_2O$–Ar complex was recorded in the region of the asymmetric-stretch $v_3$

fundamental band of $H_2O$ by Cohen *et al.* in 1988.[6] Since then the $H_2O$–Ar complex has been extensively studied using microwave,[11,12] far-IR laser,[6–8,13,14] and high resolution infrared spectroscopy.[15–18] These spectroscopic data were used to determine empirical model potential energy surfaces(PESs) directly and to test *ab initio* PESs. In 1990, two empirical intermolecular potential energy surfaces (IPSs) for $H_2O$–Ar were determined by Cohen and Saykally,[8] and Hutson[9] from tunable far-infrared laser spectroscopic data.[6] Armed with more spectroscopic data, Cohen and Saykally derived an improved PES for $H_2O$–Ar, which became known as AW2.[10] The AW2 PES has a global minimum of 142.98 cm$^{-1}$ and gave a much better description of the strong radial dependence of the anisotropic forces and of the binding energy than its predecessor (AW1).[8]

A complete understanding of the spectra requires a reliable and detailed potential energy surface. Such a surface is difficult to obtain by inverting the limited amount of experimental data. For the $H_2O$–Ar complex, five *ab initio* IPSs have been reported. In 1991, Bulski *et al.*[19] presented the first *ab initio* IPS of $H_2O$–Ar, which was computed as a sum of Heitler-London(HL) short-range repulsion energies and the long-range energies in the multipole expansion. Chalasiński *et al.*[20] calculated the *ab initio* IPS of $H_2O$–Ar by using the combination of supermolecular Møller-Plesset treatment with

the perturbation theory for long-range intermolecular forces. The potential by Chalasiński *et al.*[20] is essentially the same as that by Bulski *et al.*[19] In 1993, Tao and Klemperer reported an *ab initio* IPS for $H_2O$–Ar obtained from supermolecular calculations using fourth-order Møller-Plesset (MP4) method with efficient basis sets containing bond functions.[21] These MP4 calculations gave a single global minimum with a depth of 130.1 cm$^{-1}$. Meanwhile, Hodges *et al.* constructed the analytical ISPs for $H_2O$–Ar and $H_2O$–Ne complexes by using perturbation theory, and morphed them to accurately reproduce the interaction energies calculated at single- and double-excitation coupled-cluster theory with a noniterative perturbation treatment of triple excitations (CCSD(T)).[22] Recently, Makarewicz[23] constructed a highly accurate analytical $H_2O$–Ar IPS by calculating more than 430 single-point interaction energies at the CCSD(T) level extrapolated to the complete basis set(CBS) limit.

Although an IPS for $H_2O$–Ar that treats $H_2O$ molecule as a rigid rotor may be adequate for describing the microwave spectrum of the vibrational ground-state of $H_2O$, it cannot properly describe infrared spectra involving excitation of the intramolecular vibrational modes of $H_2O$. Recently, a four-dimensional (4D) *ab initio* potential that explicitly accounts for the bending vibrational motion was constructed and provided a good representation of experimental infrared data in the fundamental $\nu_2$ bend region of $D_2O$.[24] In 1977, Finzi *et al.*[25] observed the intramolecular vibration-vibration $(V \rightarrow V)$ transfer between the asymmetric $(\nu_3)$ and symmetric $(\nu_1)$ stretch modes of $H_2O$ to occur upon collision with Ar. Nesbitt and Lascola[16] presented spectroscopic evidence that the asymmetric and symmetric-stretch intramolecular vibrational coupling in $H_2O$ was indeed present in the $H_2O$–Ar complex, and they explained the consequences of weaker coupling between $\nu_3/\nu_1$ and the bend-stretch $\nu_2$ modes. In order to simulate the infrared transitions of $H_2O$–Ar accurately, we considered the effect of the intramolecular vibrational modes of $H_2O$ molecule when calculating the intermolecular potential.

In this work, we determined a full six-dimensional (6D) potential energy surface for the $H_2O$–Ar dimer that explicitly depends on three intramolecular vibrational modes, the $\nu_1$ symmetric-stretch, $\nu_2$ bend-stretch, and $\nu_3$ asymmetric-stretch vibrational motions of $H_2O$. The intermolecular interaction of $H_2O$–Ar is computed at the CCSD(T)/aug-cc-pVQZ level with bond functions. After vibrational averaging over three intramolecular coordinates, the resulting PESs were fitted to three-dimensional (3D) Morse/long-range (MLR) functional forms. The MLR form explicitly incorporates the theoretically known inverse-power long-range behavior and its anisotropy and dependence on the intramolecular stretch coordinates. Using these PESs, we predicted the infrared spectral transitions of the $H_2O$–Ar complex, and compared them with previous experimental and theoretical results.

This paper is arranged as follows. The *ab initio* calculation, analytic potential function form and fitting parameters are described in Sec. II. Section III presents the predictions of infrared spectra for the $H_2O$–Ar by this surface, along with a comparison to experimental results. A discussion of the results, and overall conclusions are then given in Sec. IV.

## II. POTENTIAL ENERGY SURFACE

### A. *Ab initio* calculations

The body-fixed Jacobi coordinates $(R, \theta, \phi, Q_1, Q_2, Q_3)$ used in this work are shown in Figure 1(a). $(R, \theta, \phi)$ are the intermonomer coordinates that describe the relative positions of the $H_2O$ and the Ar with $\vec{R}$ being a vector pointing from the centre of mass of the $H_2O$ to the Ar atom, $\theta$ the angle between $\vec{R}$ and the $C_2$ axis of $H_2O$, and $\phi$ the dihedral angel between the two planes defined by $\vec{R}$ with $C_2$ and the $H_2O$ molecule plane, while $Q_1$, $Q_2$, and $Q_3$ are the intramonomer coordinates which describe the symmetric stretch, bending, and asymmetric stretch modes of $H_2O$ molecule, respectively.
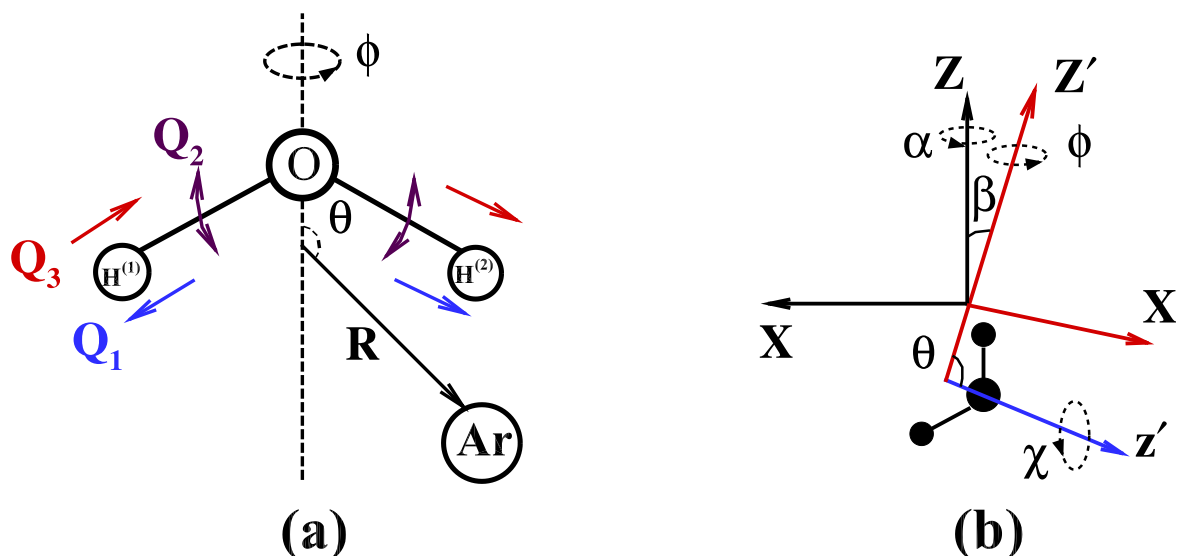


FIG. 1.  (a) Jacobi coordinates used to generate our 6D $\Delta V(R, \theta, \phi, Q_1, Q_2, Q_3)$ for $H_2O$–Ar and (b) frames used in present work to calculate the rovibrational energy levels of the *ortho*-$H_2O$–Ar and *para*-$H_2O$–Ar complexes.

On including the intramolecular vibrational coordinates $Q_1$, $Q_2$, and $Q_3$ of $H_2O$, the total potential energy for $H_2O$–Ar can be written as

$$V(R, \theta, \phi, Q_1, Q_2, Q_3) = V_{H_2O}(Q_1, Q_2, Q_3)$$
$$+ \Delta V(R, \theta, \phi, Q_1, Q_2, Q_3). \quad (1)$$

in which $V_{H_2O}(Q_1, Q_2, Q_3)$ is the 3D intramolecular potential energy surface, and $\Delta V(R, \theta, \phi, Q_1, Q_2, Q_3)$ is the 6D intermolecular interaction potential. The 3D intramolecular PES of $V_{H_2O}(Q_1, Q_2, Q_3)$ governing the $Q_1$, $Q_2$, and $Q_3$ vibration of the isolated $H_2O$ monomer was determined by Polyansky *et al.*[26] from experimental spectra data. The $Q_1$, $Q_2$, and $Q_3$ normal mode coordinates of $H_2O$ were obtained by performing geometry optimization and then frequency calculations numerically using the default procedure of MOLPRO at CCSD(T)/aug-cc-pCV5Z level of theory.

The intermolecular potential energies of $H_2O$–Ar were calculated at the CCSD(T)[27]/aug-cc-pVQZ[28] level, supplemented with an additional set of bond functions ($3s3p2d1f1g$) (where $\alpha = 0.9, 0.3, 0.1$ for $3s$ and $3p$; $\alpha = 0.6, 0.2$ for $2d$; $\alpha = 0.3$ for $f$ and $g$) placed at the mid-point of the intermolecular axis $R$.[29,30] The supermolecule approach was used to produce the intermolecular potential energy $\Delta V(R, \theta, \phi, Q_1, Q_2, Q_3)$, which is defined as the difference between the energy of the $H_2O$–Ar complex and the sum of the energies of the $H_2O$ and Ar monomers. The full counterpoise procedure was employed to correct for the basis set superposition error (BSSE).[31] All calculations were carried out using the MOLPRO package.[32]

For the 6D PESs, a total of 55 250 symmetry-unique *ab initio* points were calculated. The calculations were performed on regular grids for all six degrees of freedom. 125 potential optimized discrete variable representation(PODVR)[33,34] grid points corresponding to $Q_1 = -0.495\,35, -0.281\,76, -0.099\,34, 0.073\,81, 0.255\,34$ Å, $Q_2 = -0.581\,71, -0.290\,86, -0.030\,30, 0.227\,21, 0.509\,44$ Å and $Q_3 = -0.340\,50, -0.162\,52, 0.0, 0.162\,52, 0.340\,50$ Å were

used at for a large number of geometries on a $(R, \theta, \phi)$ grid. A relatively dense grid was used that included 13 values of $R$ (Å) = [ 3.0, 3.2, 3.4, 3.6, 3.8, 4.0, 4.2, 4.5, 5.0, 6.0, 8.0, 9.0, 10.0 ], 13 values of the polar angle $\theta$(°) evenly distributed from 0° to 180° at interval of 15°, and dihedral angles $\phi$ ranging from 0° to 90° at interval of 30°.

The 6D PES, $\Delta V(R, \theta, \phi, Q_1, Q_2, Q_3)$, of the dimer incorporates the coupling between the intermolecular $(R, \theta, \phi)$ and intramolecular $(Q_1, Q_2, Q_3)$. Since the intramolecular vibrational modes have much larger (about 100 times) frequencies than the intermolecular modes, a Born-Oppenheimer type separation may be applied. In this approximation, the full-dimension intra- and intermolecular vibrational wave functions are written as a product of monomer and intramolecular wave functions,

$$\Psi_{v_1, v_2, v_3}(R, \theta, \phi, Q_1, Q_2, Q_3) = \phi(R, \theta, \phi)\, \psi_{v_1, v_2, v_3}(Q_1, Q_2, Q_3). \quad (2)$$

Due to the weaker coupling between the $v_3/v_1$ stretching modes and the $v_2$ bending mode,[16] and the difficulty in obtaining a fully converged vibrational wave function $\psi_{v_1, v_2, v_3}(Q_1, Q_2, Q_3)$ with only a few PODVR points, we approximate $\psi_{v_1, v_2, v_3}(Q_1, Q_2, Q_3)$ in Eq. (2) with the product of $\psi_{v_1, v_3}(Q_1, Q_3)$ and $\psi_{v_2}(Q_2)$. Here, the vibrational wave functions $\psi_{v_1, v_3}(Q_1, Q_3)$ and $\psi_{v_2}(Q_2)$ are obtained by solving the following one- and two-dimensional Schrödinger equations:

$$\left[ \frac{-1}{2M_1} \frac{d^2}{dQ_1^2} + \frac{-1}{2M_3} \frac{d^2}{dQ_3^2} + V_{H_2O}(Q_1, Q_3) \right] \psi_{v_1, v_3}(Q_1, Q_3)$$
$$= E_{v_1, v_3} \psi_{v_1, v_3}(Q_1, Q_3), \quad (3)$$

$$\left[ \frac{-1}{2M_2} \frac{d^2}{dQ_2^2} + V_{H_2O}(Q_2) \right] \psi_{v_2}(Q_2) = E_{v_2} \psi_{v_2}(Q_2). \quad (4)$$

Using Eq. (2), the vibrationally averaged $H_2O$–Ar interaction potential for $H_2O$ in a given vibrational state of $(v_1, v_2, v_3)$ is

$$\Delta \overline{V}^{\{v_1, v_3\}}(R, \theta, \phi, Q_2) = \int_{-\infty}^{\infty} \psi_{v_1, v_3}^*(Q_1, Q_3) \cdot \Delta V(R, \theta, \phi, Q_1, Q_2, Q_3) \cdot \psi_{v_1, v_3}(Q_1, Q_3) dQ_1 dQ_3, \quad (5)$$

$$\Delta \overline{V}^{\{v_1, v_2, v_3\}}(R, \theta, \phi) = \int_{-\infty}^{\infty} \psi_{v_2}^*(Q_2) \cdot \Delta \overline{V}^{\{v_1, v_3\}}(R, \theta, \phi, Q_2) \cdot \psi_{v_2}(Q_2) dQ_2. \quad (6)$$

As shown in above Eqs. (5) and (6), the vibrationally averaged intermolecular potentials $\Delta \overline{V}^{\{v_1, v_2, v_3\}}(R, \theta, \phi)$ for different values of $(v_1, v_2, v_3)$ are different because the wave functions $\psi_{v_1, v_3}(Q_1, Q_3)$ and $\psi_{v_2}(Q_2)$ are associated with different vibrational quantum numbers.

## B. Analytic potential energy function

Our vibrationally averaged *ab initio* intermolecular potential energies $\Delta \overline{V}^{\{v_1, v_2, v_3\}}(R, \theta, \phi)$ for $H_2O$–Ar were fitted to a three-dimensional MLR potential function using the same

approach as Ref. 35. It may be written as follows:[35,36]

$$\Delta \overline{V}_{MLR}^{\{v_1, v_2, v_3\}}(R, \theta, \phi) = \mathfrak{D}_e(\theta, \phi)$$
$$\times \left[ 1 - \frac{u_{LR}(R, \theta, \phi)}{u_{LR}(R_e, \theta, \phi)} e^{-\beta(R, \theta, \phi) \cdot y_p^{eq}(R, \theta, \phi)} \right]^2. \quad (7)$$

In this expression, $\mathfrak{D}_e(\theta, \phi)$ the well depth, and $R_e(\theta, \phi)$ is the position of the minimum on a radial cut through the potential at the angles $\{\theta, \phi\}$, while $u_{LR}(R, \theta, \phi)$ is a function that defines the long-range behaviour of the effective 1D potential

along that cut as

$$\Delta \overline{V}^{\{v_1,v_2,v_3\}}(R,\theta,\phi) \simeq \mathfrak{D}_e(\theta,\phi) - u_{LR}(R,\theta,\phi) + \cdots. \quad (8)$$

Because $H_2O$ is polar, while Ar is non-polar, an appropriate functional form for $u_{LR}(R,\theta,\phi)$ is

$$u_{LR}(R,\theta,\phi) = \frac{\bar{C}_6(\theta,\phi)}{R^6} + \frac{\bar{C}_7(\theta,\phi)}{R^7} + \frac{\bar{C}_8(\theta,\phi)}{R^8}, \quad (9)$$

in which the long-range coefficients $\bar{C}_n$ have also been averaged over the $H_2O$ vibrational coordinates $Q_1$, $Q_2$, and $Q_3$ with the intramolecular vibrational wave function $\psi_{v_1,v_3}(Q_1,Q_3) \cdot \psi_{v_2}(Q_2)$ for each state $(v_1,v_2,v_3)$. The denominator of the second parenthetical term in Eq. (7), $u_{LR}(R_e,\theta,\phi)$ is the same function evaluated at $R = R_e(\theta,\phi)$. The radial distance variable in the exponent of Eq. (7) is a dimensionless quantity,

$$y_p^{eq}(R,\theta,\phi) = \frac{R^p - R_e(\theta,\phi)^p}{R^p + R_e(\theta,\phi)^p}, \quad (10)$$

where $p$ is a small positive integer that must be greater than the difference between the largest and smallest (inverse) powers appearing in Eq. (9), e.g., $p > (8 - 6)$. The exponent coefficient function $\beta(R,\theta,\phi)$ is a slowly varying function of $R$ and is written as a constrained polynomial of the following form:

$$\beta(R,\theta,\phi) = y_p^{ref}(R,\theta,\phi)\beta_\infty(\theta,\phi) + [1 - y_p^{ref}(R,\theta,\phi)]$$
$$\times \sum_{i=0}^{N} \beta_i(\theta,\phi) y_q^{ref}(R,\theta,\phi)^i. \quad (11)$$

The two new radial variables introduced here are

$$y_p^{ref}(R,\theta,\phi) = \frac{R^p - R_{ref}^p}{R^p + R_{ref}^p}$$

and

$$y_q^{ref}(R,\theta,\phi) = \frac{R^q - R_{ref}^q}{R^q + R_{ref}^q} \quad (12)$$

in which $R_{ref} \equiv f_{ref} \times R_e(\theta,\phi)$. Most of the previous work with this model was performed using a single radial variable to define the exponential coefficient function $\beta(R,\theta,\phi)$. In the present work, we use separate radial variable $p$ and $q$ to do our fitting. However, after we tried many values of $p$ and $q$, we found that $p = q = 3$ was the best combination, and $f_{ref} = 1.6$. The definition of $y_p^{ep}(R,\theta,\phi)$ and the algebraic structures of Eqs. (7) and (11) mean that

$$\lim_{R\to\infty} \beta(R,\theta,\phi) = \lim_{R\to\infty} \{\beta(R,\theta,\phi) \cdot y_p^{eq}(R,\theta,\phi)\}$$
$$= \beta_\infty(\theta,\phi)$$
$$= \ln\{2\mathfrak{D}_e(\theta,\phi)/u_{LR}(R_e,\theta,\phi)\}. \quad (13)$$

The parameters $\mathfrak{D}_e(\theta,\phi)$, $R_e(\theta,\phi)$, and the various exponent coefficients $\beta_i(\theta,\phi)$ all are expanded in the tesseral harmonic form

$$A(\theta,\phi) = \sum_{l=0}^{} \sum_{m=0}^{} A^{l,m} Y_l^m(\theta,\phi) \quad (14)$$

in which $A = \mathfrak{D}_e, R_e$, or $\beta_i$. The maximum value of $m$ is 6 (if $l < 6, m_{max} = l$) and $\text{mod}(m,2) = 0$.

The long-range $\bar{C}_6$ coefficients $\bar{C}_6 = \bar{C}_{6,ind} + \bar{C}_{6,disp}$, where $\bar{C}_{6,disp}$ and $\bar{C}_{6,ind}$ refer to dispersion and induction coefficients. The vibrational ground state coefficient $\overline{C}_{6,disp}^{\{0,0,0\}}$ is obtained from the experiment data,[10] using the formula given by Buckingham, Fowler, and Hutson,[37]

$$\overline{C}_{6,disp}^{\{0,0,0\}}(H_2O,Ar) \cong \frac{2\overline{C}_6^{H_2O,H_2O}\overline{\alpha}_{H_2O}\overline{C}_6^{Ar,Ar}\overline{\alpha}_{Ar}}{\overline{C}_6^{H_2O,H_2O}[\overline{\alpha}_{Ar}]^2 + \overline{C}_6^{Ar,Ar}[\overline{\alpha}_{H_2O}]^2}, \quad (15)$$

in which, $\overline{\alpha}_{Ar}$ and $\overline{\alpha}_{H_2O}$ are the polarizabilities of atomic Ar and $H_2O$, respectively, which are got from Refs. 10, 38, and 39. While the long-range coefficients for vibrationally excited states $\overline{C}_{6,disp}^{\{v_1,v_2,v_3\}}$ are estimated from

$$\overline{C}_{6,disp}^{\{v_1,v_2,v_3\}} \cong \frac{\overline{\alpha}_{H_2O}^{\{v_1,v_2,v_3\}}}{\overline{\alpha}_{H_2O}^{\{0,0,0\}}} \times \overline{C}_{6,disp}^{\{0,0,0\}}, \quad (16)$$

the $\overline{C}_{6,ind}$ is calculated from the Eq. (17)

$$\overline{C}_{6,ind} = \langle \mu_{H_2O}^2 \rangle \alpha_{Ar}. \quad (17)$$

In Eqs. (15)-(17), $\mu_{H_2O}$ and $\alpha_{H_2O}$ are the vibrational coordinates dependent upon the dipole moment and polarizability of $H_2O$, which are calculated at CCSD(T)/aug-cc-pVQZ level using the finite-field method.[40,41] The vibrationally averaged long-range coefficients $\overline{C}_{6(7,8)}(\theta,\phi)$ are expanded as

$$\overline{C}_{6(7,8)}(\theta,\phi) = \sum_{m} \overline{C}_{l=6(7,8)}^m Y_l^m(\theta,\phi). \quad (18)$$

As discussed above, the leading vibrationally averaged isotropic coefficient $\bar{C}_{6,exp}^0$ for $(0,0,0)$ ground state of $H_2O$ has been obtained from Eqs. (15) and (17). However, no angle or stretching-dependent long-range coefficients have been reported for $H_2O$–Ar complex. In this work, once we acquired the leading vibrationally averaged coefficient $\overline{C}_6^m$, the other angle dependent long-range coefficients $((l,m) \neq (6,0))$ at specific vibrationally averaged state of $(v_1,v_2,v_3)$ were then obtained by fitting the vibrationally averaged intermolecular potential with $R > 6.0$ Å to Eq. (9), while keeping $\bar{C}_6^0$ fixed at the calculated value. The final coefficient values are summarized in Table I.

## C. Least-squares fits

To begin any nonlinear least-squares fit, it is essential to choose appropriate initial trial values of the fitting parameters. The fitting parameters to the 3D-MLR form of Eq. (7) were obtained as follows. The radial R dependent energies were fitted to the ordinary 1D MLR form for all distinct combinations of $\theta$ and $\phi$ using the program betaFIT.[42] This involved some experimentation in order to ascertain the most appropriate choice for the integer parameters $p$ and $q$, and the factor $f_{ref}$ appearing in the definitions of the radial variables $y_p^{eq}(R;\theta,\phi)$, $y_p^{ref}(R;\theta,\phi)$ of Eqs. (10) and (12), and for the order N of the exponent polynomial of Eq. (11). As pointed out above, the present potential function used $p = q = 3$ and $f_{ref} = 1.6$, and the exponent polynomial order was $N = 4$.

TABLE I. Expansion coefficients $\overline{\mathfrak{D}}_e^{l,m}$ (cm$^{-1}$), $\overline{R}_e^{l,m}$ (Å), $\overline{\beta}_i^{l,m}$, and long-Range coefficients $\overline{C}_n$ (cm$^{-1}$ Å$^6$) defining our three-dimensional vibrationally averaged potential energy surfaces for $H_2O(0,0,0)$–Ar.

| | | | | | |
|---|---|---|---|---|---|
| $\overline{\mathfrak{D}}_e^{0,0}$ | 400.11 | $\overline{R}_e^{0,0}$ | 12.861 | $\overline{\beta}_0^{0,0}$ | −3.134 |
| $\overline{\mathfrak{D}}_e^{1,0}$ | −4.05 | $\overline{R}_e^{1,0}$ | −0.21 | $\overline{\beta}_0^{1,0}$ | −0.32 |
| $\overline{\mathfrak{D}}_e^{2,0}$ | 5.29 | $\overline{R}_e^{2,0}$ | 0.01 | $\overline{\beta}_0^{2,0}$ | 0.132 |
| $\overline{\mathfrak{D}}_e^{2,2}$ | 46.77 | $\overline{R}_e^{2,2}$ | −0.101 | $\overline{\beta}_0^{2,2}$ | 0.349 |
| $\overline{\mathfrak{D}}_e^{3,0}$ | −1.54 | $\overline{R}_e^{3,0}$ | 0.06 | $\overline{\beta}_0^{3,0}$ | 0.09 |
| $\overline{\mathfrak{D}}_e^{3,2}$ | −2.98 | $\overline{R}_e^{3,2}$ | −0.10 | $\overline{\beta}_0^{3,2}$ | −0.166 |
| $\overline{\mathfrak{D}}_e^{4,0}$ | −0.75 | $\overline{R}_e^{4,0}$ | −0.01 | $\overline{\beta}_0^{4,0}$ | −0.011 |
| $\overline{\mathfrak{D}}_e^{4,2}$ | 1.47 | $\overline{R}_e^{4,2}$ | 0.01 | $\overline{\beta}_0^{4,2}$ | 0.021 |
| $\overline{\mathfrak{D}}_e^{4,4}$ | 6.71 | $\overline{R}_e^{5,0}$ | −0.001 | $\overline{\beta}_0^{4,4}$ | 0.035 |
| $\overline{\mathfrak{D}}_e^{5,0}$ | 0.42 | $\overline{R}_e^{5,2}$ | 0.001 | $\overline{\beta}_0^{5,0}$ | 0.005 |
| $\overline{\mathfrak{D}}_e^{5,2}$ | −0.46 | $\overline{R}_e^{5,4}$ | −0.003 | $\overline{\beta}_0^{5,2}$ | −0.003 |
| $\overline{\mathfrak{D}}_e^{5,4}$ | 0.26 | $\overline{R}_e^{6,0}$ | −0.003 | $\overline{\beta}_0^{6,2}$ | 0.004 |
| $\overline{\mathfrak{D}}_e^{6,0}$ | 0.63 | $\overline{R}_e^{6,2}$ | −0.005 | $\overline{\beta}_0^{6,4}$ | −0.004 |
| $\overline{\mathfrak{D}}_e^{6,2}$ | −0.85 | $\overline{R}_e^{6,4}$ | −0.004 | $\overline{\beta}_1^{0,0}$ | 3.98 |
| $\overline{\mathfrak{D}}_e^{6,4}$ | 0.76 | $\overline{R}_e^{6,6}$ | −0.001 | $\overline{\beta}_1^{1,0}$ | 0.06 |
| $\overline{\mathfrak{D}}_e^{6,6}$ | 0.39 | | | $\overline{\beta}_1^{3,2}$ | 0.09 |
| | | | | $\overline{\beta}_1^{4,2}$ | −0.08 |
| | | | | $\overline{\beta}_2^{0,0}$ | 2.2 |
| | | | | $\overline{\beta}_2^{1,0}$ | 0.25 |
| | | | | $\overline{\beta}_2^{2,0}$ | 0.07 |
| | | | | $\overline{\beta}_2^{3,2}$ | 0.1 |
| | | | | $\overline{\beta}_2^{4,2}$ | −0.128 |
| | | | | $\overline{\beta}_3^{0,0}$ | 3.15 |
| | | | | $\overline{\beta}_3^{1,0}$ | 0.2 |
| | | | | $\overline{\beta}_3^{2,2}$ | 0.13 |
| $\overline{C}_6^0$ | 288 294.408 | $\overline{C}_6^2/\overline{C}_6^0$ | 1.0656 | $\overline{C}_7^4/\overline{C}_6^0$ | −0.7700 |
| | | $\overline{C}_6^4/\overline{C}_6^0$ | 0.6493 | $\overline{C}_8^0/\overline{C}_6^0$ | 199.6085 |
| | | $\overline{C}_7^0/\overline{C}_6^0$ | −1.6285 | $\overline{C}_8^2/\overline{C}_6^0$ | −61.6037 |
| | | $\overline{C}_7^2/\overline{C}_6^0$ | 0.2321 | $\overline{C}_8^4/\overline{C}_6^0$ | −37.6005 |

The resulting values of $\mathfrak{D}_e(\theta,\phi)$, $R_e(\theta,\phi)$, and $\beta_i(\theta,\phi)$ (for $i = 0 - N$) were then fitted to Eq. (14), and the resulting expansion coefficients $A^{l,m}$ were used as starting parameters in the global 3D fits to the vibrationally averaged potential energies to Eq. (7).

In the final fits, the input *ab initio* energies were weighted by assigning uncertainties of $u_i = 0.1$ cm$^{-1}$ to points in the attractive well region where $V(R,\theta,\phi) \leq 0.0$ cm$^{-1}$ and $u_i = [V(R,\theta,\phi) + 1.0]/10.0$ cm$^{-1}$ to those in the repulsive wall region where $V(R,\theta,\phi) > 0.0$ cm$^{-1}$. Using these weights, our final 58 parameters fits to 442 vibrationally averaged interaction energies below 500 cm$^{-1}$ yielded dimensionless root-mean-square (RMS) residual discrepancies of only 0.121 cm$^{-1}$. Sixteen fitting parameters were required to define $\mathfrak{D}_e(\theta,\phi)$ (see Table II), fifteen to define $R_e(\theta,\phi)$,

and 13, 4, 5, and 4 to define $\beta_i(\theta,\phi)$ for $i = 0$–3, respectively. The resulting sets of potential parameters and a FORTRAN subroutine for generating these potentials may be obtained from the authors or from the supplementary material.[43]

## D. Hamiltonian and matrix elements

Within the Born-Oppenheimer approximation, the rovibrational Hamiltonian of the $H_2O$–Ar complex formed from an "effectively rigid" vibrationally averaged $H_2O$ molecule may be written in the Jacobi coordinate system,[35,44]

$$\hat{H} = -\frac{\hbar^2}{2\mu}\frac{\partial^2}{\partial R^2} + \frac{(\hat{\vec{J}} - \hat{\vec{j}})^2}{2\mu R^2} + \hat{T}_{H_2O} + \Delta\overline{V}(R,\theta,\phi), \quad (19)$$

in which $\hat{\vec{J}}$ is the total angular momentum operator for the whole dimer, $\hat{\vec{j}}$ is the angular momentum operator of $H_2O$, $\mu$ is the reduced mass of the dimer, $\Delta\overline{V}$ is the intermolecular potential, and $\hat{T}_{H_2O}$ stands for the rigid rotor kinetic energy operator for $H_2O$,

$$\hat{T}_{H_2O} = (\frac{A+C}{2})\hat{j}^2 + [B - (\frac{A+C}{2})]\hat{j}_z^2 + (\frac{A-C}{4})(\hat{j}_+^2 + \hat{j}_-^2), \quad (20)$$

where A, B, and C are the rotational constants of $H_2O$ with the conventional definition, and $\hat{j}_\pm = \hat{j}_x \mp i\hat{j}_y$.

The total wave function used to solve the Schrödinger equation of $H_2O$–Ar complex can be written as a product of the radial and angular basis functions using the same approach as in Ref. 44. In this work, the sine discrete variable representation(DVR),[45] $R_n$, is adopted as the basis functions for the radial part. A product of eigenkets of symmetric-top rotations $|jkK\rangle|JKM\rangle$ is used as the elementary angular basis. The details of the frames used in energy levels calculations were shown in Figure 1(b), $|jkK\rangle$ describes the rotation of the water-fixed frame (WFF) $(x'\text{-}y'\text{-}z')$ in the dimer-fixed frame(DFF) $(X'\text{-}Y'\text{-}Z')$, and $|JKM\rangle$ describes the DFF rotation in the spaced-fixed frame (SFF)$(X\text{-}Y\text{-}Z)$. M is the projection of the total angular momentum J along the SFF Z-axis, and K is the projection of J along the DFF $Z'$-axis, while k stands for projection of the $H_2O$ angular momentum j onto the WFF $z'$-axis (the $C_2$ axis). The $|jkK\rangle$ and $|JKM\rangle$ are set to share the same K value because $H_2O$ is the only source of rotation about the $Z'$-axis. Our elementary angular basis $|jkK\rangle|JKM\rangle$ can be combined to give a parity-adapted basis,[46]

$$|\Theta_{jkK}^{JMP}\rangle = \frac{1}{\sqrt{2(1 + \delta_{k,0}\delta_{K,0})}}$$
$$\times [|jkKJM\rangle + (-1)^{J+k+P}|j-k-KJM\rangle], \quad (21)$$

where the space-inversion parity $P = 0$ or 1 denoting whether the basis is even or odd under inversion. Here, only J and P are rigorously good quantum numbers. The parity of k determines whether $H_2O$ is para or ortho.[44,47,48] Then, the $(-1)^{J+P}$ being even or odd, gives rovibrational states e or f symmetry, respectively. The eigenvalues and eigenvectors are obtained through the same approach as in Ref. 44. All states of concern in this work have principal K values

TABLE II. Properties of stationary points of the $H_2O$–Ar potential energy surface and comparisons with results from previously reported surfaces. All entries are given as $\{R\ (\text{Å}),\ \theta°,\ \phi°,\ \Delta V\ (\text{cm}^{-1})\}$, in which some $\phi$ are given "···," it means that $\phi$ can be an arbitrary value from 0.0° to 360.0°.

|  | Global minimum | In-plane barriers | Out-plane barrier |
|---|---|---|---|
| $V_{\text{MLR}}(0,0,0)$ | {3.630, 100.5, 0.0, −139.529} | {3.565, 0.0, …, 26.053} <br> {3.681, 180.0, …, 20.582} | {3.685, 90.0, 90.0, 49.680} |
| $V_{\text{MLR}}(0,0,1)$ | {3.643, 100.1, 0.0, −142.237} | {3.559, 0.0, …, 26.231} <br> {3.713, 180.0, …, 23.371} | {3.682, 90.0, 90.0, 50.610} |
| AW2[10] | {3.518, 105.7, 0.0, −142.98} | {3.702, 0.0, …, 26.29} <br> {3.636, 180.0, …, 17.18} |  |
| $V_{\text{MP4}}$[21] | {3.603, 105.0, 0.0, −130.2} | {3.620, 0.0, …, 26.6} <br> {3.711, 180.0, …, 22.6} | {3.757, 90.0, 90.0, 52.6} |
| $V_{\text{CBS}}$[23] | {3.695, 111.0, 0.0, −141.2} | {3.51, 0.0, …, 26.1} <br> {3.72, 180.0, …, 20.3} | {3.70, 90.0, 90.0, 50.5} |

of 0 or 1 on the intermolecular axis, denoted as $\sum$ and $\prod$ states. For the $j_{k_ak_c}$ assignment, we simply apply the projection operators for the eigenstate into the $|jkK\rangle$ basis.[44] The projection operators $|0_{00}\rangle\langle 0_{00}|$, $|1_{10}\rangle\langle 1_{10}|$, $|1_{11}\rangle\langle 1_{11}|$, and $|1_{01}\rangle\langle 1_{01}|$ are then used to pick out the corresponding components from the eigenstate. Presently, we use the $H_2O$ ground-state experimental values for the rotational constants ($A = 27.8806$ cm$^{-1}$, $B = 14.5216$ cm$^{-1}$, and $C = 9.2778$ cm$^{-1}$).[49] For the $\nu_3 = 1$ state of $H_2O$, we choose the A, B, C of $H_2O$ to exactly reproduce the experimental values $\nu_3 = 3755.9287$ cm$^{-1}$ ($A = 26.6303$ cm$^{-1}$, $B = 14.4225$ cm$^{-1}$ and $C = 9.1418$ cm$^{-1}$).[50] The masses of H, O, and Ar atoms were chosen to be 1.007 825 032 07, 15.994 915, and 39.962 590 98 u, respectively. In our calculations, we used 50 sine DVR grid points for the $R$ coordinate ranging from 4.0 $a_0$ to 30.0 $a_0$. For the angular coordinates, 13 Gaussian-Legendre and 13 Gaussian-Chebyshev quadrature points were used for the numerical integration over $\theta$ and $\phi$. The treatment of the matrix element of potential $\Delta\overline{V}$ is also briefly described in the Appendix of Ref. 44.

## III. RESULTS AND DISCUSSION

### A. Features of the three-dimensional potential energy surface

Figure 2 shows the contour plots of the vibrationally averaged 3D $V_{\text{MLR}}$ ground-state potential energy surface for $H_2O$ (0,0,0)–Ar in Jacobi coordinates. Figure 2(a) presents how the minimum energy surface depends on $\theta$ and $R$ when $\phi$ is optimized to minimize the energy for each ($\theta$, $R$). As seen in Figure 2(a), the global minimum with a well depth of 139.53 cm$^{-1}$ is located at ($\theta = 100.5°$, $\phi = 0.0°$, $R = 3.630$ Å), which is in a planar T-shape geometry with the argon in the $H_2O$ molecular plane ($\phi = 0.0°$), and one of the hydrogens is nearest to argon. Figure 2(b) presents how the minimum energy surface depends on $\theta$ and $\phi$ when $R$ is optimized to an energy minimum. As shown in Figure 2(b), the two equivalent global minima with $\phi = 0.0°$ and $\phi = 180.0°$ (by symmetry) are connected by an out-plane barrier which is located at ($\theta = 95.3°$, $\phi = 90.0°$, and $R = 3.69$ Å), with a barrier of height 49.883 cm$^{-1}$ relative to the global minima. Geometries
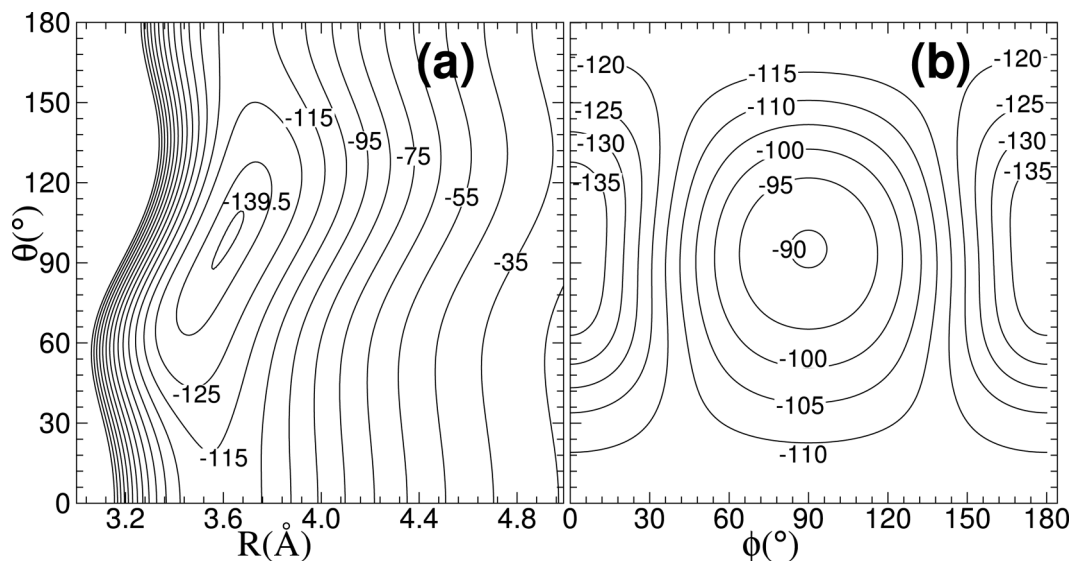


FIG. 2. Contour plots(in cm$^{-1}$) of the minimum energy surface on our vibrationally averaged 3D $V_{\text{MLR}}(0,0,0)$ PES for $H_2O(0,0,0)$–Ar: (a) as a function of angle $\theta$ and $R$ for optimized value of $\phi$ and (b) as a function of $\theta$ and $\phi$ for optimized value of $R$.

with the argon in the molecular plane ($\phi = 0°$, or $180.0°$) are more favorable than out of plane structures. Figure 2(b) also shows that another two in-plane barriers joining the two equivalent global minima. One of the in-plane barriers is located at ($R = 3.565$ Å, $\theta = 0°$) with energy of $-113.48$ cm$^{-1}$, and another one is located at ($R = 3.681$ Å, $\theta = 180°$) with energy of $-118.95$ cm$^{-1}$. These two in-plane barriers lie on the $C_2$ axis, and thus there is no energy dependence on the angle $\phi$.

Figure 3 illustrates the energy (upper) and radial position (lower) along the minimum energy path which joins the two in-plane saddle points to the global minimum. As can be seen in Figure 3, the barriers for in-plane rotation are 26.05 cm$^{-1}$ at $\theta = 0°$ and 20.58 cm$^{-1}$ at $\theta = 180°$. It is interesting to notice that the smallest radial position occurs at $\theta = 58.0°$ along the minimum energy path, which is far from the minimum.

Table II summarizes the geometries and energies of these global minima along with barriers of $V_{MLR}$ PES for H$_2$O–Ar complex, all of which can be compared with previous literature results for this system.[10,21,23] Overall, our results are consistent with previous empirical and *ab initio* surfaces, showing essentially the same anisotropy and similar interaction strength. On our 3D $V_{MLR}$ PES, the well depth at the global minimum recovers 98% of the AW2 well depth and is only 1.67 cm$^{-1}$ shallower than that of the most accurate *ab initio* $V_{CBS}$ surface.[23] The barrier for out-plane rotation at ($\theta = 90.0°$, $\phi = 90.0°$) is 49.68 cm$^{-1}$, which is in good agreement with 50.5 cm$^{-1}$ of $V_{CBS}$.[23]


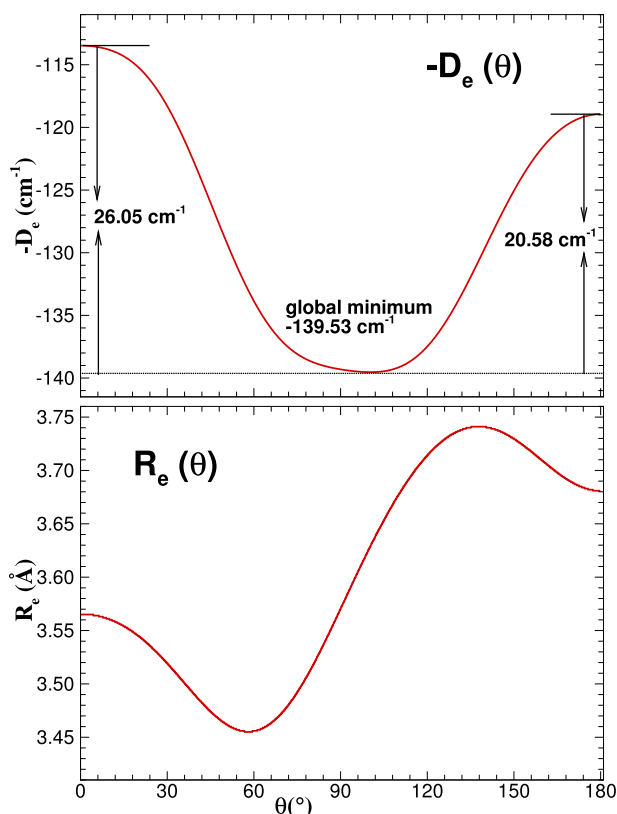
FIG. 3. Energy (upper) and radial position (lower) along the minimum energy path on our vibrationally averaged 3D $V_{MLR}$ PES for H$_2$O(0, 0, 0)–Ar as functions of angle $\theta$ for optimized values of $\phi$ and $R$.

For the vibrationally averaged excited-state $(0,0,1)$ surface, the contour plots look almost the same as those for the ground state $(0,0,0)$. As shown by comparison of the first two cases in Table II, the positions and energies of the stationary points are only slightly shifted.

## B. Bound states and band origin shifts

The calculated rovibrational energy levels with $(v_1, v_2, v_3) = (0, 0, 0)$ are listed in Table III for *para*-H$_2$O–Ar and *ortho*-H$_2$O–Ar. The rovibrational energy levels are labeled with six quantum numbers $(J, j_{k_a k_c}, K, k, P, n_s)$ in free internal rotor model, where $J$ is the total angular momentum for the whole complex, $j_{k_a k_c}$ denotes the asymmetric top level of the H$_2$O subunit, $K$ is the projection of $J$ on the intermolecular axis, where $K = 0$ or $K = 1$ is corresponding to $\sum$ or $\prod$ state, $k$ is the projection of $j$ on the $C_2$ axis of H$_2$O molecule in which the evenness and oddness of $k$ determine *para*-H$_2$O–Ar or *ortho*-H$_2$O–Ar complex, $P$ stands for the parity e or f symmetry with $P = (-1)^J$ or $P = (-1)^{J+1}$, and $n_s$ is the radial stretching quantum number.

Table III lists the energies of the ($J = 0$ and $J = 1$) intermolecular rovibrational energy levels for *para*-H$_2$O–Ar and *ortho*-H$_2$O–Ar generated from our 3D $V_{MLR}$ PESs, and compares them with results obtained from the AW2 PES.[10] It is clear from this table that all the bound states of our 3D $V_{MLR}$ PESs have shallower energy levels than those of the AW2 PES. For *para*-H$_2$O–Ar, the lowest rovibrational energy for the ground state is $-93.494$ cm$^{-1}$ indicating that the zero-point energy is 46.035 cm$^{-1}$, about 1/3 of the global well depth $D_e$ (139.529 cm$^{-1}$). The zero-point energy of *para*-H$_2$O–Ar is significantly higher than the in-plane barriers of 26.05 and 20.58 cm$^{-1}$, which indicates that the ground state wave function is highly delocalized.

For *ortho*-H$_2$O–Ar, the energies of the bound states are lower than the asymptote of *ortho*-H$_2$O with $j_{k_a k_c} = 1_{01}$ with energy of 23.799 cm$^{-1}$, which is calculated from the sum of the rotational constants $B + C$ of H$_2$O. As seen in Table III, the lowest bound state energy is $-76.646$ cm$^{-1}$, and the dissociation energy is 100.445 cm$^{-1}$ for *ortho*-H$_2$O–Ar, which is about 7 cm$^{-1}$ larger than the dissociation energy of 93.494 cm$^{-1}$ for *para*-H$_2$O–Ar. Therefore, *ortho*-H$_2$O–Ar is more stable than *para*-H$_2$O–Ar.

In order to test the effect of the intramolecular vibrational motion $(Q_1, Q_2, Q_3)$ and their coupling on the intermolecular potential of $\Delta \overline{V}(R, \theta, \phi)$, the band origin shifts associated with three fundamental bands of $v_1$, $v_2$, and $v_3$ of H$_2$O are predicted from our vibrational averaged 3D $V_{MLR}$ PESs, which are obtained by averaging over our 4D $\Delta V(R, \theta, \phi, Q_{1,2,3})$, 5D $\Delta V(R, \theta, \phi, Q_1, Q_3)$, and 6D $\Delta V(R, \theta, \phi, Q_1, Q_2, Q_3)$ intermolecular potentials, respectively. Table IV lists all the predicted shifts $\Delta v_1$, $\Delta v_2$, and $\Delta v_3$ from different reduced-dimension treatments, and can compares them with the corresponding experimental values obtained using some approximations.[16,17]

For *para*-H$_2$O–Ar, on our 4D PES with three intermolecular coordinates $V(R, \theta, \phi)$ and one intramolecular normal-mode coordinate ($Q_1$, $Q_2$ or $Q_3$) for corresponding vibrational excitation of the H$_2$O, the calculated shifts are

TABLE III. Energies (in $cm^{-1}$) for the rovibrational levels of our vibrationally averaged 3D $V_{MLR}$ PESs for $H_2O$–Ar expressed relative to the relevant asymptote and compared with previous results obtained from AW2 PES.[10]

| | | *para*-$H_2O$–Ar | | | | | *ortho*-$H_2O$–Ar | | | |
|---|---|---|---|---|---|---|---|---|---|---|
| Assignment | AW2 | 3D $V_{MLR}$ | AW2 | 3D $V_{MLR}$ | Assignment | AW2 | 3D $V_{MLR}$ | AW2 | 3D $V_{MLR}$ |
| | $J=0, P=0$ | | $J=1, P=1$ | | | $J=0, P=0$ | | $J=1, P=1$ | |
| $n_s=0, \sum(0_{00})$ | −98.330 | −93.494 | −98.130 | −93.296 | $n_s=0, \sum(1_{01})$ | −81.583 | −76.646 | −81.388 | −76.453 |
| $n_s=1, \sum(0_{00})$ | −68.083 | −63.776 | −67.892 | −63.588 | $n_s=0, \prod(1_{01})$ | | | −70.031 | −65.229 |
| $n_s=0, \prod(1_{11})$ | | | −61.293 | −56.433 | $n_s=0, \prod(1_{10})$ | | | −60.307 | −55.429 |
| $n_s=0, \sum(1_{11})$ | −57.650 | −53.223 | −57.451 | −53.022 | $n_s=1, \sum(1_{01})$ | −47.608 | −43.547 | −47.427 | −43.366 |
| $n_s=2, \sum(0_{00})$ | −39.253 | −36.151 | −39.084 | −35.986 | $n_s=1, \prod(1_{01})$ | | | −36.706 | −32.871 |
| $n_s=0, \sum/\prod(2_{02})$ | | | −33.091 | −28.514 | $n_s=1, \prod(1_{10})$ | | | −25.801 | −21.767 |
| $n_s=0, \sum/\prod(2_{02})$ | −32.858 | −28.264 | −32.246 | −27.716 | $n_s=0, \sum(2_{12})$ | −25.007 | −20.425 | −24.854 | −20.273 |
| $n_s=1, \sum(1_{11})$ | −27.130 | −23.562 | −26.984 | −23.409 | $n_s=0, \prod(2_{12})$ | | | −20.200 | −15.419 |
| $n_s=1, \prod(1_{11})$ | | | −24.481 | −19.884 | $n_s=2, \sum(1_{01})$ | −15.981 | −12.061 | −15.803 | −11.880 |
| $n_s=3, \sum(0_{00})$ | −18.177 | −16.172 | −18.033 | −16.028 | $n_s=2, \prod(1_{01})$ | | | −10.511 | −7.959 |
| | $J=0, P=1$ | | $J=1, P=0$ | | | $J=0, P=1$ | | $J=1, P=0$ | |
| $n_s=0, \prod(1_{11})$ | | | −61.285 | −56.421 | $n_s=0, \prod(1_{01})$ | | | −70.038 | −65.236 |
| $n_s=0, \prod(2_{02})$ | | | −32.674 | −28.156 | $n_s=0, \prod(1_{10})$ | | | −60.312 | −55.434 |
| $n_s=1, \prod(1_{11})$ | | | −24.507 | −19.903 | $n_s=0, \sum(1_{10})$ | −45.424 | −40.845 | −45.223 | −40.645 |
| | | | | | $n_s=1, \prod(1_{01})$ | | | −36.712 | −32.877 |
| | | | | | $n_s=1, \prod(1_{10})$ | | | −25.805 | −21.771 |
| | | | | | $n_s=1, \prod(2_{12})$ | | | −20.222 | −15.430 |
| | | | | | $n_s=1, \sum(1_{10})$ | −13.352 | −10.229 | −13.170 | −10.049 |

shown in column 2 of Table IV. As seen there, $\Delta v_1$ and $\Delta v_2$ calculated on 4D PES for *para*-$H_2O$–Ar are equal to −1.684 and −0.659 $cm^{-1}$, which are in good agreement with the values of −1.675 and −0.671 $cm^{-1}$ in column 6 of Table IV calculated on full dimension PES, which includes all 3 intermolecular coordinates and 3 intramolecular normal-mode coordinates. The discrepancies are smaller than 0.012 $cm^{-1}$. Meanwhile, the predicted $\Delta v_3$ on 4D PES is −0.049 $cm^{-1}$, which is about two orders of magnitude smaller than the value of −1.999 $cm^{-1}$ from our 6D PES. If we take into account both of $Q_1$ and $Q_3$ coordinates, the predicted $\Delta v_3$ on 5D $\Delta V(R, \theta, \phi, Q_1, Q_3)$ PES is −2.041 $cm^{-1}$, which is then significantly decreased and in good agreement with the value of −1.999 $cm^{-1}$ obtained from full dimension PES. These phenomena can be explained by

the significant difference between the averaged values of the symmetric normal coordinate of $Q_1$ for the vibrational ground (0, 0, 0) and first-excited (0, 0, 1) states of the anti-symmetric vibration of $v_3$ mode,

$$\langle 0,0,0|Q_1|0,0,0\rangle = -0.039 \text{ Å}, \quad (22)$$

$$\langle 0,0,1|Q_1|0,0,1\rangle = -0.082 \text{ Å}. \quad (23)$$

In contrast, the averaged values of the anti-symmetric normal coordinate of $Q_3$ for the vibrational ground (0, 0, 0) and first-excited (1, 0, 0) states of the symmetric vibration of $v_1$ mode are both very small and differ vey little,

$$\langle 0,0,0|Q_3|0,0,0\rangle = 0.005 \text{ Å}, \quad (24)$$

$$\langle 1,0,0|Q_3|1,0,0\rangle = 0.000 \text{ Å}, \quad (25)$$

so the $v_3$ mode will not affect the shift of the $v_1$ fundamental transition. These phenomena have been found and pointed out by our previous studies on $CO_2$–He or $H_2$ systems, too.[51,52] The predicted $\Delta v_3$ shift on our full dimension PES is 0.28 $cm^{-1}$ smaller than the experimental value of −1.72 $cm^{-1}$,[16] which was approximately obtained by averaging two origins of $\sum(0_{00}, v_3 = 1) \leftarrow \prod(1_{01}, v_3 = 0)$ and $\prod(1_{01}, v_3 = 1) \leftarrow \sum(0_{00}, v_3 = 0)$, and neglecting the differences of vibrational excitation on the intermolecular potential; more details were discussed in Ref. 16.

However, the predicted $\Delta v_2$ on 4D PES is −0.659 $cm^{-1}$, which is almost in the same accuracy as the value of −0.671 $cm^{-1}$ obtained from full dimension PES and is also in good agreement with experimental value of −0.58 $cm^{-1}$.[17] Because for the fundamental $v_2$ transition (0, 0, 0) ← (0, 1, 0) of $H_2O$–Ar, the averaged values of the $Q_1$ and $Q_3$ for the vibrational ground (0, 0, 0) and excited (0, 1, 0) states are

TABLE IV. The band origin shifts (in $cm^{-1}$) associated with three fundamental bands of $v_1$, $v_2$ and $v_3$ of *para*-$H_2O$–Ar and *ortho*-$H_2O$–Ar are calculated from our vibrational averaged 3D $V_{MLR}$ PESs, which are obtained by averaging over 4D $\Delta V(R, \theta, \phi, Q_{1,2 \text{ or } 3})$, 5D $\Delta V(R, \theta, \phi, Q_1, Q_3)$, or full 6D $\Delta V(R, \theta, \phi, Q_1, Q_2, Q_3)$ intermolecular potential, respectively. The predicted shifts are compared with experiment values Refs. 16 and 17, in which $\Delta v_3$ shift of −1.72 $cm^{-1}$,[16] was approximately obtained by averaging two origins of $\sum(0_{00}, v_3 = 1) \leftarrow \prod(1_{01}, v_3 = 0)$ and $\prod(1_{01}, v_3 = 1) \leftarrow \sum(0_{00}, v_3 = 0)$ neglecting the differences of vibrational excitation on the intermolecular potential.

| | *para*-$H_2O$–Ar | | | | *ortho*-$H_2O$–Ar | | |
|---|---|---|---|---|---|---|---|
| | 4D | 5D | 6D | Exp. | 4D | 5D | 6D |
| $\Delta v_1$ | −1.684 | −1.729 | −1.675 | | −2.236 | −2.047 | −2.266 |
| $\Delta v_2$ | −0.659 | | −0.671 | −0.58[a] | −0.880 | | −0.913 |
| $\Delta v_3$ | −0.049 | −2.041 | −1.999 | −1.72[b] | −0.244 | −2.285 | −2.506 |

[a]Reference 17.
[b]Reference 16.

again almost the same,

$$\langle 0,0,0|Q_1|0,0,0\rangle = -0.039 \text{ Å}, \tag{26}$$

$$\langle 0,1,0|Q_1|0,1,0\rangle = -0.031 \text{ Å}, \tag{27}$$

and

$$\langle 0,0,0|Q_3|0,0,0\rangle = 0.005 \text{ Å}, \tag{28}$$

$$\langle 0,1,0|Q_3|0,1,0\rangle = 0.000 \text{ Å}, \tag{29}$$

respectively, which indicates that the fundamental $v_2$ transition $(0, 0, 0) \rightarrow (0, 1, 0)$ has very little dependence on the $Q_1$ and $Q_3$ coordinates. Thus, only taking into account the intramolecular $Q_2$ coordinate of $H_2O$, the calculated vibrational frequency shift of $-0.659$ cm$^{-1}$ on the 4D PES is comparable with that value of $-0.671$ cm$^{-1}$ obtained on the full 6D PES.

All predicted shifts are red shifts, which explicitly indicates the evidence for the intra- and inter-molecular vibrational couplings. The shifts values directly reflect the strength of the couplings. All shifts of *ortho*-$H_2O$–Ar are larger than the corresponding values of *para*-$H_2O$–Ar, due to stronger binding energy of *ortho*-$H_2O$–Ar than that of *para*-$H_2O$–Ar.

As shown in Table IV, with or without intramolecular bend-stretch of the $Q_2$ coordinate, there are no significant differences in the vibrational frequency shifts of $\Delta v_3$ for both *para*-$H_2O$–Ar and *ortho*-$H_2O$–Ar. This provides further evidence of the weaker coupling between the $v_3/v_1$ and the $v_2$ modes for the $H_2O$–Ar dimer. When we calculate the frequency shifts of $\Delta v_3$ for $H_2O$–Ar complex, we cannot ignore the symmetric stretch $Q_1$ coordinate. A 5D $\Delta V(R, \theta, \phi, Q_1, Q_3)$ PES that explicitly accounts for the asymmetric-stretch $Q_3$ and symmetric stretch $Q_1$ coordinates is necessary to describe $v_3$ vibrational motion of $H_2O$, due to the different averaged values of the $Q_1$ for two vibrational states of the fundamental $v_3$ transition of $H_2O$. The results are agreement with the experimental observations,[16,25] and the present conclusions about intermode coupling are consistent with those form
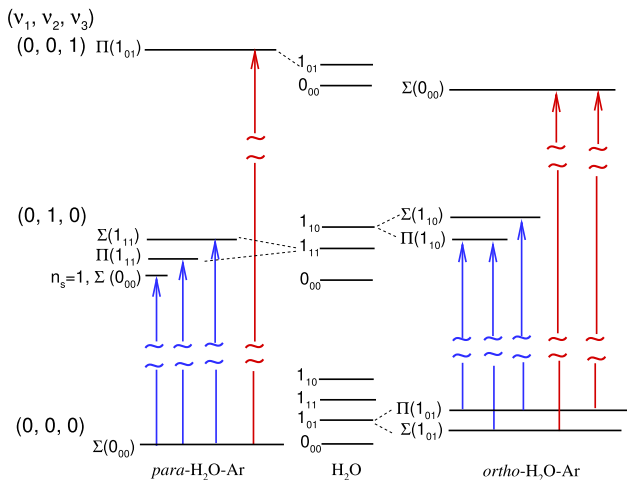
previous theoretical treatments of $CO_2$ with He or $H_2$ complexes.[51,53,54]

## C. Predicted infrared spectra

Infrared $(v_1, v_2, v_3) = (0, 0, 1) \leftarrow (0, 0, 0)$ transition energies for *para*-$H_2O$–Ar and *ortho*-$H_2O$–Ar calculated from our vibrationally averaged 3D PESs obtained by averaging over the full dimension $\Delta V(R, \theta, \phi, Q_1, Q_2, Q_3)$ intermolecular potential, are listed and compared with the experimental results observed by Lascola and Nesbitt.[15,16] The rotational levels were assigned using the labels $J$, $j_{K_aK_c}$ and $K$, as discussed in Sec. III B. Schematic display of the allowed infrared transitions bands in the $v_3 = 1 \leftarrow 0$ antisymmetric stretch excitation region for *para*-$H_2O$–Ar and *ortho*-$H_2O$–Ar is shown in Figure 4.

For *para*-$H_2O$–Ar, Table V expresses the infrared transition energies relative to the 3782.5429 cm$^{-1}$ transition energy[16] of $\prod(1_{01}, v_3 = 1) \leftarrow \sum(0_{00}, v_3 = 0)$. Column 2 lists



(v$_1$, v$_2$, v$_3$)

FIG. 4. Schematic displaying of the energy levels of free-rotor $H_2O$ and internal rotor energy levels in $H_2O$–Ar complex. In the $v_3 = 1 \leftarrow 0$ antisymmetric stretch excitation region, three allowed bands are shown in red lines, and in the $v_2 = 1 \leftarrow 0$ bending stretch excitation region, a total of 6 allowed bands are drew in blue lines.

TABLE V. Infrared $(v_1, v_2, v_3) = (0, 0, 1) \leftarrow (0, 0, 0)$ transition energies (in cm$^{-1}$) of *para*-$H_2O$–Ar calculated from our vibrationally averaged 3D $V_{MLR}(R, \theta, \phi)$ PESs obtained by averaging over full dimension $\Delta V(R, \theta, \phi, Q_1, Q_2, Q_3)$ intermolecular potential and comparisons with experiment. Frequencies are relative to the 3782.5429 cm$^{-1}$ transition[16] of $\prod(1_{01}, 1) \leftarrow \sum(0_{00}, 0)$ (labeled with $K(j_{k_ak_c}, v_3)$).

| Levels $J' - J''$ | Observed | Calculated | Difference |
|---|---|---|---|
| | | *R* branch | |
| 1–0 | 0.000 | 0.000 | 0.000 |
| 2–1 | 0.207 | 0.205 | 0.002 |
| 3–2 | 0.417 | 0.412 | 0.005 |
| 4–3 | 0.631 | 0.623 | 0.008 |
| 5–4 | 0.847 | 0.836 | 0.011 |
| 6–5 | 1.068 | 1.051 | 0.017 |
| 7–6 | 1.293 | 1.269 | 0.024 |
| 8–7 | 1.519 | 1.488 | 0.031 |
| | | *P* branch | |
| 1–2 | −0.598 | −0.593 | −0.005 |
| 2–3 | −0.790 | −0.784 | −0.006 |
| 3–4 | −0.977 | −0.971 | −0.006 |
| 4–5 | −1.161 | −1.155 | −0.005 |
| 5–6 | −1.341 | −1.336 | −0.005 |
| 6–7 | −1.516 | −1.513 | −0.003 |
| 7–8 | −1.686 | −1.687 | 0.001 |
| 8–9 | −1.855 | −1.858 | 0.004 |
| 9–10 | −2.023 | −2.027 | 0.005 |
| | | *Q* branch | |
| 1–1 | −0.206 | −0.204 | −0.002 |
| 2–2 | −0.212 | −0.211 | −0.002 |
| 3–3 | −0.222 | −0.220 | −0.002 |
| 4–4 | −0.235 | −0.232 | −0.002 |
| 5–5 | −0.253 | −0.248 | −0.004 |
| 6–6 | −0.264 | −0.268 | 0.004 |
| 7–7 | −0.293 | −0.291 | −0.002 |
| 8–8 | −0.322 | −0.317 | −0.005 |
| 9–9 | −0.358 | −0.348 | −0.010 |
| 10–10 | −0.405 | −0.383 | −0.022 |
| RMSD | | | 0.010 |

the experimental results from Ref. 16, and Column 3 is the calculated transitions from our vibrationally averaged 3D $V_{MLR}$ PESs. The differences for the total of 27 transitions, including P, Q, and R branch patterns are presented in column 4. These differences are very small, and the root mean square discrepancy of only 0.10 cm$^{-1}$ indicates that our PESs are able to provide a good representation of the experimental data.

For *ortho*-H$_2$O–Ar, Table VI expresses all the infrared transition energies relative to the 3738.0058 cm$^{-1}$ monomer transition $\sum(0_{00}, v_3 = 1) \leftarrow \sum(1_{01}, v_3 = 0)$ and the 3726.2722 cm$^{-1}$ monomer transition $\sum(0_{00}, v_3 = 1) \leftarrow$

$\prod(1_{01}, v_3 = 0)$. Columns 3 and 6 show the transition energies yielded by our vibrationally averaged 3D $V_{MLR}$ PESs, which are in good agreement with the experimental values shown in columns 2 and 5.[15] The differences seen in columns 4 and 7 are very small, and the rms discrepancies for a total of 25 and 35 bound state transitions are only 0.010 and 0.017 cm$^{-1}$, respectively.

For the bend-stretch excitation $(v_1, v_2, v_3) = (0, 1, 0) \leftarrow (0, 0, 0)$, the infrared transition energies for *para*-H$_2$O–Ar and *ortho*-H$_2$O–Ar were also calculated from our vibrationally averaged 3D $V_{MLR}$ PESs obtained by averaging over full-

TABLE VI. Infrared $(v_1, v_2, v_3) = (0, 0, 1) \rightarrow (0, 0, 0)$ transition energies (in cm$^{-1}$) of *ortho*-H$_2$O–Ar calculated from our vibrationally averaged 3D $V_{MLR}(R, \theta, \phi)$ PESs obtained by averaging over full dimension $\Delta V(R, \theta, \phi, Q_1, Q_2, Q_3)$ intermolecular potential and comparisons with experiment. All the frequencies are relative to the 3738.0058 cm$^{-1}$ transition[15] of $\sum(0_{00}, 1) \leftarrow \sum(1_{01}, 0)$ and the 3726.2722 cm$^{-1}$ transition[15] of $\sum(0_{00}, 1) \leftarrow \prod(1_{01}, 0)$ (labeled with $K(j_{k_a k_c}, v_3)$).

| Levels $J' - J''$ | $\sum(0_{00}, 1) \leftarrow \sum(1_{01}, 0)$ | | | $\sum(0_{00}, 1) \leftarrow \prod(1_{01}, 0)$ | | |
|---|---|---|---|---|---|---|
| | Observed | Calculated | Difference | Observed | Calculated | Difference |
| *P* branch | | | | | | |
| 0–1 | −0.393 | −0.390 | −0.003 | 0.000 | 0.000 | 0.000 |
| 1–2 | −0.583 | −0.579 | −0.004 | −0.208 | −0.207 | −0.001 |
| 2–3 | −0.769 | −0.764 | −0.005 | −0.422 | −0.418 | −0.004 |
| 3–4 | −0.950 | −0.944 | −0.006 | −0.641 | −0.633 | −0.007 |
| 4–5 | −1.127 | −1.120 | −0.006 | −0.864 | −0.853 | −0.011 |
| 5–6 | −1.300 | −1.292 | −0.008 | −1.091 | −1.077 | −0.015 |
| 6–7 | −1.468 | −1.460 | −0.008 | −1.322 | −1.304 | −0.019 |
| 7–8 | −1.632 | −1.624 | −0.009 | −1.557 | −1.534 | −0.024 |
| 8–9 | −1.793 | −1.784 | −0.009 | −1.795 | −1.767 | −0.028 |
| 9–10 | −1.949 | −1.940 | −0.009 | −2.035 | −2.003 | −0.033 |
| 10–11 | −2.102 | −2.092 | −0.009 | −2.279 | −2.241 | −0.038 |
| 11–12 | −2.251 | −2.241 | −0.009 | −2.524 | −2.481 | −0.044 |
| 12–13 | −2.398 | −2.387 | −0.011 | | | |
| *R* branch | | | | | | |
| 1–0 | 0.000 | 0.000 | 0.000 | | | |
| 2–1 | 0.203 | 0.202 | 0.001 | 0.596 | 0.592 | 0.004 |
| 3–2 | 0.409 | 0.407 | 0.002 | 0.784 | 0.780 | 0.005 |
| 4–3 | 0.620 | 0.616 | 0.004 | 0.966 | 0.962 | 0.004 |
| 5–4 | 0.835 | 0.829 | 0.005 | 1.144 | 1.140 | 0.004 |
| 6–5 | 1.053 | 1.046 | 0.008 | 1.316 | 1.313 | 0.003 |
| 7–6 | 1.275 | 1.265 | 0.010 | 1.484 | 1.481 | 0.003 |
| 8–7 | 1.500 | 1.488 | 0.011 | 1.646 | 1.645 | 0.001 |
| 9–8 | 1.728 | 1.714 | 0.014 | 1.804 | 1.804 | 0.000 |
| 10–9 | 1.959 | 1.942 | 0.017 | 1.957 | 1.959 | −0.002 |
| 11–10 | 2.191 | 2.172 | 0.019 | 2.104 | 2.109 | −0.005 |
| 12–11 | 2.424 | 2.404 | 0.020 | 2.248 | 2.256 | −0.008 |
| *Q* branch | | | | | | |
| 1–1 | | | | 0.206 | 0.204 | 0.002 |
| 2–2 | | | | 0.209 | 0.208 | 0.001 |
| 3–3 | | | | 0.214 | 0.215 | −0.001 |
| 4–4 | | | | 0.220 | 0.223 | −0.003 |
| 5–5 | | | | 0.229 | 0.233 | −0.005 |
| 6–6 | | | | 0.239 | 0.246 | −0.007 |
| 7–7 | | | | 0.253 | 0.261 | −0.009 |
| 8–8 | | | | 0.266 | 0.279 | −0.013 |
| 9–9 | | | | 0.282 | 0.299 | −0.016 |
| 10–10 | | | | 0.302 | 0.321 | −0.020 |
| 11–11 | | | | 0.322 | 0.346 | −0.024 |
| 12–12 | | | | 0.345 | 0.374 | −0.030 |
| RMSD | | | 0.010 | | | 0.017 |

dimension $\Delta V(R, \theta, \phi, Q_1, Q_2, Q_3)$ intermolecular potential and are listed and compared with the experimental data of Lascola and Nesbitt[17] in Tables S4 and S5 of the supplementary material.[43] As seen in columns 3, 6, and 9 of Table S4,[43] the transition frequencies of *para*-$H_2O$–Ar are relative to the 1625.3520 cm$^{-1}$ monomer transition[17] $n_s = 1, \sum(0_{00}, v_2 = 1) \leftarrow \sum(0_{00}, v_2 = 0)$, the 1634.2034 cm$^{-1}$ transition[17] $\prod(1_{11}, v_2 = 1) \leftarrow \sum(0_{00}, v_2 = 0)$ and the 1637.3610 cm$^{-1}$ transition[17] $\sum(1_{11}, v_2 = 1) \leftarrow \sum(0_{00}, v_2 = 0)$. The differences seen in columns 4, 7, and 10 are very small, yielding RMS discrepancies of only 0.006 cm$^{-1}$, 0.056 cm$^{-1}$ and 0.051 cm$^{-1}$, respectively. For *ortho*-$H_2O$–Ar, transition frequencies calculated from our 3D $V_{MLR}$ PESs are shown in the columns 3, 6, 9, and 12 of Table S5.[43] The transition frequencies are relative to the 1606.6715 cm$^{-1}$ monomer transition[17] $\prod(1_{10}, v_2 = 1) \leftarrow \prod^e(1_{01}, v_2 = 0)$, the 1606.6877 cm$^{-1}$ transition[17] $\prod(1_{10}, v_2 = 1) \leftarrow \prod^f(1_{01}, v_2 = 0)$, the 1618.6128 cm$^{-1}$ transition[17] $\prod(1_{10}) \leftarrow \sum(1_{01})$, and the 1622.4695 cm$^{-1}$ transition[17] $\sum(1_{10}, v_2 = 1) \leftarrow \prod(1_{01}, v_2 = 0)$. The RMS discrepancies listed in the last line of Table S5[43] are only 0.030 cm$^{-1}$, 0.045 cm$^{-1}$, 0.049 cm$^{-1}$ and 0.013 cm$^{-1}$, respectively. Again, the good agreement between predicted infrared spectra and experimental observations for fundamental bend-stretch excitation further confirms the high accuracy of our potential energy surface.

## IV. CONCLUSION

In this paper, we have presented an accurate $H_2O$–Ar potential energy surface that includes explicit dependence on the $Q_1$, $Q_2$, and $Q_3$ normal coordinates of the $H_2O$ molecule. This potential energy surface is based on *ab initio* interaction energies obtained at the CCSD(T) level with a large aug-cc-pVQZ basis set, and with bond functions placed at the mid-point on the intermolecular axis. The vibrationally averaged potential energies were fitted to a 3D MLR potential form that incorporates the theoretically known long-range inverse-power behaviour.[35,36,55] Having this correct long-range behavior is very important and is necessary to provide a good description of a $H_2O$ molecule in medium to large sized $(Ar)_N$ clusters, as was the case for $CO_2$, CO, or OCS doped in $(He)_N$[51,56] or $(para$-$H_2)_N$[52,57] clusters. The global 3D fit to the 442 vibrationally averaged interaction energies had a RMS residual discrepancy of only 0.013 cm$^{-1}$, and required only 58 parameters for each of case.

The PESs have been employed to compute the rovibrational energy levels for *para*-$H_2O$–Ar and *ortho*-$H_2O$–Ar complexes using the radial DVR/angular FBR method. The calculated band origin shifts on a full 6D intra- and intermolecular PES associated with the three fundamental transitions of $H_2O$ for both *para*-$H_2O$–Ar and *ortho*-$H_2O$–Ar were predicted for the first time and are in good agreement with the experimental values, as summarized in Table IV. The values of the frequency shifts for the three fundamental transitions are different, which reflects the strengths of the coupling induced by the intramolecular vibrational modes ($v_1$, $v_2$, and $v_3$). The coupling interactions induced by symmetric stretch/antisymmetric stretch modes are almost

three times stronger than those induced by the bending stretch mode. Most importantly, the comparison of the vibrational frequency shifts on including vs. neglecting the effect of one or both of the other intramolecular vibrational coordinates provide clear evidence of the origin, extent and strength of the coupling between different vibrational modes. The results indicate that there exists weak coupling between symmetric and antisymmetric stretch ($v_1/v_3$) modes and the bending-stretch $v_2$ mode in the $H_2O$–Ar complex, while there is strong coupling between the symmetric stretch $v_1$ and antisymmetric stretch $v_3$ modes themselves. This can be explained by the significant difference between the averaged values of the symmetric $Q_1$ coordinate for the ground $(0, 0, 0)$ and excited $(0, 0, 1)$ states of the fundamental $v_3$ transition, while for the fundamental $v_2$ transition, the averaged values of $Q_1$ and $Q_3$ for the vibrational ground $(0, 0, 0)$ and excited $(0, 1, 0)$ states are almost the same. Therefore, if one simulates the spectra and dynamics of $H_2O$ doped in $(Ar)_N$ clusters (even within large clusters of $^4$He), the adiabatic separation of bending coordinate $(Q_2)$ of $H_2O$ from the symmetric and antisymmetric stretch coordinates ($Q_1$ and $Q_3$) is a reasonable approximation for a reduced-dimension treatment, and we believe that this will not introduce serious errors. On the other hand, if one wishes to study the antisymmetric stretch $v_3$ vibrational motion of $H_2O$ in doped clusters or matrix environments, it will be necessary to take into account both the asymmetric-stretch $Q_3$ and symmetric stretch $Q_1$ coordinates simultaneously.

Infrared spectra of *ortho*-$H_2O$–Ar and *para*-$H_2O$–Ar complexes were also predicted on the vibrational quantum-state-specific PESs. Comparison with the computational and experimental data for $H_2O$–Ar demonstrates the high quality of the present PES: for three bands of asymmetric stretch $(v_1, v_2, v_3) = (0, 0, 1) \leftarrow (0, 0, 0)$ transitions of *para*- and *ortho*-$H_2O$–Ar, the rms discrepancies are only 0.010 cm$^{-1}$ for $\prod(1_{01}) \leftarrow \sum(0_{00})$ of *para*-$H_2O$–Ar, 0.017 cm$^{-1}$ and 0.010 cm$^{-1}$ for $\sum(0_{00}) \leftarrow \prod(1_{01})$ and $\sum(0_{00}) \leftarrow \sum(1_{01})$ of *ortho*-$H_2O$–Ar, respectively.

This work should serve as a good starting point for studying the spectra and energy transfer dynamics of $H_2O$ doped in Ar clusters and will be useful for future studies of the influence of temperature and matrix environments.

## ACKNOWLEDGMENTS

[1]K. Ramasesha, L. De Marco, A. Mandal, and A. Tokmakoff, Nat. Chem. **5**, 935 (2013).
[2]M. L. Cowan, B. D. Bruner, N. Huse, J. R. Dwyer, B. Chugh, E. T. J. Nibbering, T. Elsaesser, and R. J. D. Miller, Nature **434**, 199 (2005).
[3]D. Kraemer, M. L. Cowan, A. Paarmann, N. Huse, E. T. J. Nibbering, T. Elsaesser, and R. J. D. Miller, Proc. Natl. Acad. Sci. U. S. A. **105**, 437 (2008).

[4]C. S. William and H. C. Andersen, J. Phys. Chem. **88**, 6548 (1984).

[5]K. Watanabe and H. C. Andersen, J. Phys. Chem. **90**, 795 (1986).

[6]R. C. Cohen, K. L. Busarow, K. B. Laughlin, G. A. Blake, M. Havenith, Y. T. Lee, and R. J. Saykally, J. Chem. Phys. **89**, 4494 (1988).

[7]R. C. Cohen, K. L. Busarow, Y. T. Lee, and R. J. Saykally, J. Chem. Phys. **92**, 169 (1990).

[8]R. C. Cohen and R. J. Saykally, J. Phys. Chem. **94**, 7991 (1990).

[9]J. M. Hutson, J. Chem. Phys. **92**, 157 (1990).

[10]R. C. Cohen and R. J. Saykally, J. Chem. Phys. **98**, 6007 (1993).

[11]G. T. Fraser, F. J. Lovas, R. D. Suenram, and K. Matsumura, J. Mol. Spectrosc. **144**, 97 (1990).

[12]T. C. Germann and H. S. Gutowsky, J. Chem. Phys. **98**, 5235 (1993).

[13]R. C. Cohen and R. J. Saykally, J. Chem. Phys. **95**, 7891 (1991).

[14]S. Suzuki, R. E. Bumgarner, P. A. Stockman, P. G. Green, and G. A. Blake, J. Chem. Phys. **94**, 824 (1991).

[15]R. Lascola and D. J. Nesbitt, J. Chem. Phys. **95**, 7917 (1991).

[16]D. J. Nesbitt and R. Lascola, J. Chem. Phys. **97**, 8096 (1992).

[17]M. J. Weida and D. J. Nesbitt, J. Chem. Phys. **106**, 3078 (1997).

[18]X. C. Liu and Y. J. Xu, J. Mol. Spectrosc. **301**, 1 (2014).

[19]M. Bulski, P. E. S. Wormer, and A. van der Avoird, J. Chem. Phys. **94**, 8096 (1991).

[20]G. Chalasinski, M. M. Szczsniak, and S. Scheiner, J. Chem. Phys. **94**, 2807 (1991).

[21]F. M. Tao and W. Klemperer, J. Chem. Phys. **101**, 1129 (1994).

[22]M. P. Hodges, R. J. Wheatley, and A. H. Harvey, J. Chem. Phys. **117**, 7169 (2002).

[23]J. Makarewicz, J. Chem. Phys. **129**, 184310 (2008).

[24]S. Wang, S. He, L. Dai, E. Feng, and W. Huang, J. Chem. Phys. **142**, 224307 (2015).

[25]J. Finzi, F. E. Hovis, V. N. Panfilov, P. Hess, and C. B. Moore, J. Chem. Phys. **67**, 4053 (1977).

[26]O. L. Polyansky, P. Jensen, and J. Tennyson, J. Chem. Phys. **105**, 6490 (1996).

[27]K. Raghavachari, G. W. Trucks, J. A. Pople, and M. Head-Gordon, Chem. Phys. Lett. **157**, 479 (1989).

[28]D. E. Woon and T. H. Dunning, Jr., J. Chem. Phys. **98**, 1358 (1993).

[29]F. M. Tao and Y. K. Pan, Mol. Phys. **81**, 507 (1994).

[30]T. B. Pedersen, B. Fernandez, H. Koch, and J. Makarewicz, J. Chem. Phys. **115**, 8431 (2001).

[31]S. F. Boys and F. Bernardi, Mol. Phys. **19**, 553 (1970).

[32]H. J. Werner, P. J. Knowles, R. D. Amos, A. Berning, D. L. Cooper, M. J. O. Deegan, A. J. Dobbyn, F. Eckert, S. T. Elbert, C. Hampel, R. Lindh, A. W. Lloyd, W. Meyer, A. Nicklass, K. Peterson, R. Pitzer, A. J. Stone, P. R. Taylor, M. E. Mura, P. Pulay, M. Schutz, H. Stoll, and

T. Thoorsteinsso, MOLPRO, version 2010.1, a package of *ab initio* programs, 2010, see http://www.molpro.net.

[33]H. Wei and T. Carrington, J. Chem. Phys. **97**, 3029 (1992).

[34]J. Echave and D. C. Clary, Chem. Phys. Lett. **190**, 225 (1992).

[35]Y. T. Ma, T. Zeng, and H. Li, J. Chem. Phys. **140**, 214309 (2014).

[36]R. J. Le Roy, Y. Huang, and C. Jary, J. Chem. Phys. **125**, 164310 (2006).

[37]A. D. Buckingham, P. W. Fowler, and J. M. Hutson, Chem. Rev. **88**, 963 (1988).

[38]K. T. Tang, J. M. Norbeck, and P. R. Certain, J. Chem. Phys. **64**, 3063 (1976).

[39]E. A. Reinsch and W. Meyer, Phys. Rev. A **14**, 915 (1976).

[40]H. D. Cohen and C. C. J. Roothaan, J. Chem. Phys. **43**, 34 (1965).

[41]H. Li and R. J. Le Roy, J. Chem. Phys. **126**, 224301 (2007).

[42]R. J. Le Roy, betaFIT 2.0: A Computer Program to Fit Potential Function Points to Selected Analytic Functions, University of Waterloo Chemical Physics Research Report CP-665, 2009, see http://leroy.uwaterloo.ca/programs/.

[43]See supplementary material at http://dx.doi.org/10.1063/1.4939089 for In Tables S1–S3 of the supplementary material, we show the parameters defining the three-dimensional vibrationally averaged potential energy surfaces for $H_2O$–Ar complexes with $H_2O$ at vibrational excited states of $(0, 0, 1)$, $(0, 1, 0)$, and $(1, 0, 0)$, and a FORTRAN subroutine for generating those 3D potentials. The predicted infrared $(v_1, v_2, v_3)$ $= (0, 1, 0) \leftarrow (0, 0, 0)$ transition energies (in $cm^{-1}$) of *para*-$H_2O$–Ar and *ortho*-$H_2O$–Ar are listed in Tables S4 and S5.

[44]T. Zeng, H. Li, R. J. L. Roy, and P.-N. Roy, J. Chem. Phys. **135**, 094304 (2011).

[45]D. T. Colbert and W. H. Miller, J. Chem. Phys. **96**, 1982 (1992).

[46]L. Wang and M. H. Yang, J. Chem. Phys. **129**, 174305 (2008).

[47]X. G. Wang and T. Carrington, Jr., J. Chem. Phys. **134**, 044313 (2011).

[48]A. van der Avoird and D. J. Nesbitt, J. Chem. Phys. **134**, 044314 (2011).

[49]F. C. DeLucia, P. Helminger, R. L. Cook, and W. Gordy, Phys. Rev. A **5**, 487 (1972).

[50]R. A. Toth, J. Mol. Spectrosc. **194**, 28 (1999).

[51]H. Li, N. Blinov, P.-N. Roy, and R. J. Le Roy, J. Chem. Phys. **130**, 144305 (2009).

[52]H. Li, R. J. Le Roy, P.-N. Roy, and A. R. W. McKellar, Phys. Rev. Lett. **105**, 133401 (2010).

[53]H. Li and R. J. Le Roy, Phys. Chem. Chem. Phys. **10**, 4128 (2008).

[54]H. Li, P.-N. Roy, and R. J. Le Roy, J. Chem. Phys. **132**, 214309 (2010).

[55]R. J. Le Roy and R. D. E. Henderson, Mol. Phys. **105**, 663 (2007).

[56]H. Li and Y.-T. Ma, J. Chem. Phys. **137**, 234310 (2012).

[57]P. L. Raston, W. Jager, H. Li, R. J. Le Roy, and P.-N. Roy, Phys. Rev. Lett. **108**, 253402 (2012).